Group connectivity in COSMOS: a tracer of mass assembly history

E. Darragh Ford,[1,2]⋆ C. Laigle,[2]⋆ G. Gozaliasl [ORCID],[3,4,5] C. Pichon,[6,7,8] J. Devriendt,[2]
A. Slyz,[2] S. Arnouts,[9] Y. Dubois,[6] A. Finoguenov,[3,4] R. Griffiths,[10] K. Kraljic,[7]
H. Pan,[2,11] S. Peirani[12] and F. Sarron[6]

[1]*Department of Physics, University of Chicago, 5640 South Ellis Avenue, ERC 569, Chicago, IL 60637, USA*
[2]*Sub-department of Astrophysics, University of Oxford, Keble Road, Oxford OX1 3RH, UK*
[3]*Finnish Centre for Astronomy with ESO (FINCA), Quantum, Vesilinnantie 5, University of Turku, FI-20014 Turku, Finland*
[4]*Department of Physics, University of Helsinki, PO Box 64, FI-00014 Helsinki, Finland*
[5]*Helsinki Institute of Physics, University of Helsinki, P.O. Box 64, FI-00014 Helsinki, Finland*
[6]*Institut d'Astrophysique de Paris, Sorbonne Universités, UPMC Univ Paris 6 et CNRS, UMR 7095, 98 bis bd Arago, 75014 Paris, France*
[7]*Institute for Astronomy, University of Edinburgh, Royal Observatory, Blackford Hill, Edinburgh EH9 3HJ, UK*
[8]*Korea Institute for Advanced Study (KIAS), 85 Hoegiro, Dongdaemun-gu, Seoul 02455, Republic of Korea*
[9]*Aix Marseille Université, CNRS, CNES, LAM, 38 rue F. Joliot Curie, F-13388, Marseille, France*
[10]*Department of Physics and Astronomy, University of Hawaii at Hilo, 200 W. Kawili St, Hilo, HI 96720, USA*
[11]*University of Chinese Academy of Sciences, Beijing 100049, China*
[12]*Observatoire de la Côte d'Azur, Université Côte d'Azur, CNRS, Laboratoire Lagrange, Bd de l'Observatoire, CS 34229, F-06304 Nice Cedex 4, France*

ABSTRACT

Cosmic filaments are the channel through which galaxy groups assemble their mass. Cosmic connectivity, namely the number of filaments connected to a given group, is therefore expected to be an important ingredient in shaping group properties. The local connectivity is measured in COSMOS around X-ray-detected groups between redshift 0.5 and 1.2. To this end, large-scale filaments are extracted using the accurate photometric redshifts of the COSMOS2015 catalogue in two-dimensional slices of thickness 120 comoving Mpc centred on the group's redshift. The link between connectivity, group mass, and the properties of the brightest group galaxy (BGG) is investigated. The same measurement is carried out on mocks extracted from the light-cone of the hydrodynamical simulation HORIZON-AGN in order to control systematics. More massive groups are on average more connected. At fixed group mass in low-mass groups, BGG mass is slightly enhanced at high connectivity, while in high-mass groups BGG mass is lower at higher connectivity. Groups with a star-forming BGG have on average a lower connectivity at given mass. From the analysis of the HORIZON-AGN simulation, we postulate that different connectivities trace different paths of group mass assembly: at high group mass, groups with higher connectivity are more likely to have grown through a recent major merger, which might be in turn the reason for the quenching of the BGG. Future large-field photometric surveys, such as *Euclid* and LSST, will be able to confirm and extend these results by probing a wider mass range and a larger variety of environment.

Key words: methods: numerical – methods: observational – galaxies: evolution – galaxies: formation – galaxies: photometry – large-scale structure of Universe.

1 INTRODUCTION

In the local Universe, a large fraction of the stellar mass resides in galaxy groups and clusters. These environments are the place of a wide variety of quenching processes, mostly depending on the

group mass, leading to different galaxy population contents (e.g. Peng et al. 2010, 2012; Gobat et al. 2015; Treyer et al. 2018). These processes are first connected to the availability and physical state of the intra-cluster gas. The infalling cold gas can be gravitationally heated (e.g. Birnboim & Dekel 2003; Kereš et al. 2005), maintained hot via feedback from active galaxy nuclei (AGNs, Dubois et al. 2013), and therefore is not available anymore for accretion and star formation. Other processes are related to interactions between gas and galaxies, such as ram-pressure stripping (Gunn & Gott 1972),

⋆ E-mail: elise.darragh-ford.17@alumni.ucl.ac.uk (EDF); laigle@iap.fr (CL)

or between galaxies, including galaxy mergers, galaxy harassment (Moore et al. 1996), tidal interactions (Byrd & Valtonen 1990; Hahn et al. 2009), and some are more specific to the cluster or group infall regions, i.e. outside the virial radius (see e.g. Sarron et al. 2019; Salerno, Martínez & Muriel 2019). In addition, the infalling gas in the group or cluster can be diverted towards the central galaxy or its satellites, depending on their relative mass (e.g. Simha et al. 2009) and the relaxation state of the group, a process often leading to satellite quenching by starvation (e.g. Van de Voort et al. 2017) due to tidal effect in the neighbourhood of the most massive galaxy.

Groups are not isolated structures but they keep accreting matter – including small galaxies, but also gas (Kauffmann, Li & Heckman 2010) – from the large-scale cosmic web they are connected to. Therefore, investigating the link between the large-scale cosmic web and group properties is an essential question for galaxy formation and also cosmology. On the one hand, the mean number of filaments branching out from groups – namely their local connectivity – depends on the growth factor and therefore the Dark Energy equation of state. Precise measurement of this quantity provides a topologically robust alternative to constrain cosmology, as it can be shown to depend on moments of the hierarchy of the N-point correlation functions (Codis, Pogosyan & Pichon 2018). The disconnection of filaments with cosmic time is driven both by gravitational clustering and by dark energy which will stretch and disconnect neighbouring filaments through the increased expansion of voids.

On the other hand, the geometry and anisotropy of the large-scale environment is connected to the nature, history, and dynamics of matter infall, knowledge of which, in turn, is essential to shape the mass assembly of groups and clusters. Several works have already emphasized the link between the large-scale environment and the properties of groups and their central galaxies (e.g. Scudder, Ellison & Mendel 2012; Luparello et al. 2015; Zehavi et al. 2018), although some others conclude in the absence of correlation for high-mass haloes (Jung, Lee & Yi 2014). The variety of definitions for the large-scale environment can be one of the reasons for these conflicting conclusions. On a similar note, the measured correlation between the quenching of the central galaxy and the fraction of quenched satellites in the group, introduced as 'galactic conformity' by Weinmann et al. (2006), and either confirmed or debated since then (e.g. Kauffmann et al. 2013; Hartley et al. 2015; Hearin, Behroozi & van den Bosch 2016; Treyer et al. 2018), can be interpreted as an environmental process, in which the properties of both central and satellite galaxies of a given group depend on the mass assembly history of their host halo, which depends on the large-scale environment. In fact, the geometry of matter infall on groups being for the most part filamentary, this environmental question must be addressed primarily from the perspective of the cosmic web.

The question of the role of the cosmic web has been quite actively investigated in recent years, but mainly from the point of view of how isolated galaxies are affected by the cosmic structure they inhabit, or by the distance to their nearest cosmic filaments or nodes. Correlations have been found between proximity to a filament and galaxy type, mass, colour, and star formation rate. More specifically, galaxies residing closer to a filament tend to be more massive, have lower star formation rates and H I contents (e.g. Alpaslan et al. 2016; Chen et al. 2017; Crone Odekon et al. 2018; Kraljic et al. 2018; Luber et al. 2019), although this topic is still debated (see e.g. Kleiner et al. 2017, for a different claim), possibly owing to the different scales and mass ranges considered. However, several questions about the influence of the cosmic web geometry on galaxy

groups remain unanswered: where do the groups sit in the cosmic web as a function of their mass? Can the filaments penetrate deeply into haloes and preferentially feed the central galaxies, or are the satellites bringing in all the accreted gas? What fraction of the mass load and the angular momentum is advected by how many filaments (e.g. Pichon et al. 2011; Tillson, Miller & Devriendt 2011; Danovich et al. 2012, 2015)? How can we understand cosmic connectivity as a function of node mass? How is (stellar or AGN) feedback correlated to or impacted by the number of connected filaments? Observationally, detecting filaments around groups is an essential first step to address these questions.

This quest has therefore raised the interest of many and is now a growing field of investigation, with various methods of filament detections, including weak lensing (Dietrich et al. 2005; Jauzac et al. 2012; Gouin et al. 2017), stacking thermal Sunyaev–Zel'dovich detection (Bonjean et al. 2018) or galaxy overdensity (Zhang et al. 2013) between clusters pairs, X-ray emission (Dietrich et al. 2012; Parekh et al. 2017), or measurement of the local elongation spotted in the galaxy density distribution (Darvish et al. 2015; Durret et al. 2016). Beyond trying to understand the process of mass assembly in the largest virialized structures of the Universe, the motivation for hunting matter in filaments is also to create a comprehensive census of the baryonic matter in the Universe. Although these first detections are encouraging, a more systematic study is needed in order to draw statistically significant conclusions on the impact of the large-scale environment on galaxy group properties. These studies require a complete catalogue of accurate galaxy redshifts in order to precisely identify filaments, and a volume large enough to host both a significant number of massive structures and a large variety of large-scale environments. Large spectroscopic surveys are promising for this purpose, but are for now limited to low redshift (see e.g. Poudel et al. 2017, for a study in the SDSS). An alternative is to rely on photometric data. As shown in Laigle et al. (2018), filaments can be reliably extracted from photometric redshifts by relying on two-dimensional slices, the thickness of which is calibrated based on the typical redshift accuracy. As an example, extracting filaments from photometric redshifts around massive clusters has been already successfully done in the CFHTLS T0007 data (Sarron et al. 2019) at low redshift ($0.15 < z < 0.70$).

In this work, we rely on the wealth of photometric data from the COSMOS field to perform the filament extraction around intermediate-mass groups at higher redshift, and we use a robust group catalogue which has been extracted from X-ray photometry (Finoguenov et al. 2007; Gozaliasl et al. 2019). The correlation between group connectivity, group mass, and the brightest group galaxy (BGG) properties is first quantified both in the observations and the corresponding mocks. In the second step, the HORIZON suite (Dubois et al. 2014) is used to interpret the observational results. The paper is organized as follows: Section 2 describes the observed and simulated data sets and the tools used to extract the skeleton. Section 3 presents the measurements both from the observed and simulated catalogues, and an extensive assessment of the robustness of the results. Section 4 provides an interpretation of the observational results based on the HORIZON-AGN simulation. Section 5 summarizes the results and outlines future works. Appendix A gives more details on the connectivity measurement in the simulation and in COSMOS. We use a standard ΛCDM cosmology with a Hubble constant $H_0 = 70.4 \, \mathrm{km \, s^{-1} \, Mpc^{-1}}$, total matter density $\Omega_m = 0.272$, and dark energy density $\Omega_\Lambda = 0.728$. Unless specified otherwise, errorbars are the errors on the mean derived from bootstrap resampling.

2 DATA SET AND EXTRACTION METHODS

Let us first present briefly the observational data set, the simulations and the ridge extraction tools used to quantify the connectivity of groups, and the robustness of this extraction with respect to photometric redshift uncertainty.

2.1 The COSMOS data set

The analysis presented here is based on the COSMOS data set (Scoville et al. 2007). The cosmic web is extracted using the photometric redshift of the COSMOS2015 catalogue (Laigle et al. 2016), which is also used for deriving galaxy masses. Groups are extracted from the X-ray photometry as described in Finoguenov et al. (2007) and Gozaliasl et al. (2019). The observed catalogue of groups, their associated BGG and filaments in COSMOS is called $\mathscr{C}_{cosmos}$ in the following analysis.

2.1.1 COSMOS2015 redshifts and stellar masses

The COSMOS2015 catalogue provides apparent magnitudes in 30 bands from ultraviolet (UV) to infrared (IR). The photometric data include the optical COSMOS-20 Subaru survey (Capak et al. 2007; Ilbert et al. 2009), Subaru Suprime-Cam data (Taniguchi et al. 2007, 2015), the u^*-band data from the Canada–Hawaii–France Telescope (CFHT/MegaCam), NIR photometry from the UltraVISTA survey (DR2, McCracken et al. 2012), the Y band from the Hyper Suprime-Cam at Subaru telescope (Miyazaki et al. 2012), and mid-IR data in the four IRAC channels (i.e. in a wavelength range between ∼3 and 8 µm) from the SPLASH program (PI: Capak). Galaxy photometry in optical and NIR has been extracted using SEXTRACTOR (Bertin & Arnouts 1996) in dual image mode, using as the detection image a χ^2 sum of the four NIR images of UltraVISTA DR2 and the z^{++}-band (taken with Subaru Suprime-Cam). We removed from the catalogue all the objects which are flagged as belonging to a polluted area or for which the photometry is possibly contaminated by the light of saturated stars, meaning that only objects in $\mathscr{A}^{UVISTA} \& \mathscr{A}^{!OPT} \& \mathscr{A}^{COSMOS}$ are kept, according to the notations in table 7 of Laigle et al. (2016).

Photometric redshifts (photo-z), stellar masses, and absolute magnitudes have been computed using LEPHARE (Arnouts et al. 2002; Ilbert et al. 2006) with a configuration similar to Ilbert et al. (2013). The stellar mass completeness of the sample is estimated from the K_s magnitude following Pozzetti et al. (2010). At redshift $z = 1.2$, the sample is 90 per cent complete down to $M_{lim} = 10^{9.2}$ M$_\odot$. However, in this work, only galaxies more massive than 10^{10} M$_\odot$ are used to extract the filament distribution over the redshift range $0.5 < z < 1.2$. Because our analysis relies on a global extraction of the filaments – in contrast to previous works which are based on a local search around groups – a large enough comoving area is required, which sets the lower limit of our redshift range to $z \sim 0.5$. The upper limit is defined by the rapid increase of the redshift uncertainties at $z \sim 1.2$ (see fig. 14 of Laigle et al. 2016).[1]

A large spectroscopic redshift catalogue is also available on the COSMOS field, as a result of the common effort of several spectroscopic follow-up campaigns since 2007 (e.g. Lilly et al. 2007; Kartaltepe et al. 2010; Comparat et al. 2015; Le Fèvre et al. 2015). This spectroscopic sample is essential for the calibration of
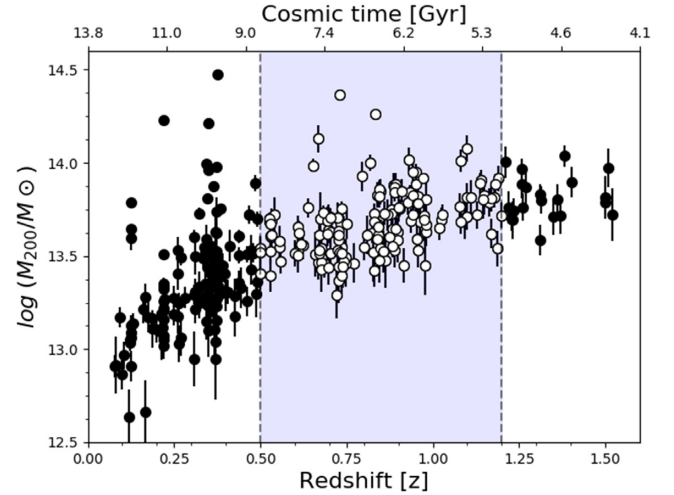
---

[1] A consequence of the shift of the Balmer break in NIR broad-bands.

Figure 1. The halo mass of X-ray groups (M_{200}) in the COSMOS field as a function of redshift (filled and open circles). The highlighted area represents the groups with a redshift range of $0.5 < z < 1.2$, which is used in this study (open circles).

the photometric redshifts and for a better determination of group redshifts.

2.1.2 The X-ray group catalogue

The initial catalogues of the X-ray galaxy groups in COSMOS were presented in Finoguenov et al. (2007) and George et al. (2011). These catalogues combined the available *Chandra* and *XMM–Newton* data (with improvements in the photometric data sets) used for identification of galaxy groups, with confident identification reaching out to $z \sim 1.0$. The COSMOS galaxy group catalogue we rely on is a combination of an updated version of the initial group catalogues and a new catalogue of 73 groups described in Gozaliasl et al. (2019) and Gozaliasl et al., in preparation, which combines data of all X-ray observations from *Chandra* and *XMM–Newton* in the 0.5–2 keV band, with robust group identification up to $z \sim 1.53$. However, for the purpose of this study and for the reason explained above, we limit our selection to $z \sim 0.5$–1.2 (highlighted area in Fig. 1).

Group halo mass is the total mass (commonly called M_{200}, but we call it M_{group} in the rest of this paper), determined using the scaling relation L_X–M_{200} with weak lensing mass calibration as presented by Leauthaud et al. (2010). The radius of the group R_{200} is defined as the radius enclosing M_{200} with a mean overdensity of $\Delta \sim 200$ times the critical background density. Fig. 1 presents the group mass log ($M_{200}/M_\odot$) as function of the redshift and cosmic time. Gozaliasl et al. (2019) discussed the mass completeness of the group sample given the surface brightness limitation of the X-ray data set. Over the redshift range $0.5 < z < 1.2$, the evolution of the group mass limit is weak and lies within the observational uncertainties, being around log $M_{group}/M_\odot \sim 13.38$ at $z \sim 0.5$ and log $M_{group}/M_\odot \sim 13.5$ at $z \sim 1.2$.

The redshift of the group is the redshift of the peak of the galaxy distribution within the group radius, while slicing the light-cone with a redshift step of 0.05. In most cases, this redshift determination is strengthened by the presence of spectroscopic redshifts. The BGG is identified from the COSMOS2015 photometry as being the most massive galaxy within R_{200}, with a redshift that agrees with that of the hosting group (Gozaliasl et al. 2019). More than

Table 1. A summary of all the catalogues used in this study, the data selection, the group and CW extraction methods, and the persistence thresholds used in DisPerSE.

Name	Data	Group selection	z and mass ranges	CW extraction and persistence	Comments
$\mathscr{C}_{\text{cosmos}}$	COSMOS field	X-ray	$0.5 < z < 1.2$	in 2D slices (120 Mpc), 1.5σ	photo-z and
	1.38 deg^2	86 groups	$13.38 < \log M_{\text{group}}/M_\odot$	from galaxies, $M_* > 10^{10}\,M_\odot$	masses
$\mathscr{C}_{\text{Hzagn 2D}}^{\text{phot}}$	HORIZON-AGN light-cone	ADAPTAHOP	$0.5 < z < 1.2$	in 2D slices (120 Mpc), 1.5σ	photo-z and
	1 deg^2	76 groups	$13.3 < \log M_{\text{group}}/M_\odot$	from galaxies, $M_* > 10^{10}\,M_\odot$	masses
$\mathscr{C}_{\text{Hzagn 2D}}^{\text{true}}$	HORIZON-AGN light-cone	ADAPTAHOP	$0.5 < z < 1.2$	in 2D slices (120 Mpc), 1.5σ	intrinsic-z
	1 deg^2	76 groups	$13.3 < \log M_{\text{group}}/M_\odot$	from galaxies, $M_* > 10^{10}\,M_\odot$	and masses
$\mathscr{C}_{\text{Hzagn 3D}}$	HORIZON-AGN snapshots	ADAPTAHOP	three snapshots, $z = 0.63,\ 0.81,\ 1.03$	in 3D, 5σ	intrinsic-z
	3×100^3 (Mpc/h)^3	1115 groups	$13.0 < \log M_{\text{group}}/M_\odot$	from all DM haloes	and masses

~ 80 per cent of the BGGs have secure spectroscopic redshifts. Group centres from the X-ray emission are determined with an accuracy of $\sim$5 arcsec, using the smaller scale emission detected by *Chandra* data. The BGG does not always sit at the peak of the X-ray centre emission. As described in Gozaliasl et al. (2019), the off-central BGG probably resides in groups which are more likely to have experienced a recent halo merger.

As described in Gozaliasl et al. (2019), a quality flag has been assigned to each group depending on the robustness of the extraction and the potential availability of spectroscopic redshift. In our study, we keep only group with a flag of 1, 2, and 3. Over the redshift range $0.5 < z < 1.2$ and considering only groups with BGG galaxies more massive than $\log M_*/M_\odot = 10$ and in a non-flagged area, we are left with 86 groups containing around 900 galaxies, over 1.38 deg^2 (or $\sim$62 groups per square degree).

2.2 The HORIZON-AGN simulation

The HORIZON-AGN[2] (Dubois et al. 2014) cosmological hydrodynamical simulation is used both to assess the quality of the observational measurements and to provide an interpretative framework. Therefore, several catalogues are built from the simulation. We first use the mock catalogue which has been generated from the HORIZON-AGN simulated light-cone. Two versions of this catalogue are built: $\mathscr{C}_{\text{Hzagn 2D}}^{\text{phot}}$ and $\mathscr{C}_{\text{Hzagn 2D}}^{\text{true}}$, for which cosmic web filaments are extracted either from the photometric quantities (redshift and masses, Laigle et al. 2019) or intrinsic ones, respectively. Comparing the results from these catalogues allows to quantify the impact of photometric noise and to assess the quality of the connectivity measurement from observations (Section 2.4).

Furthermore, in order to interpret the data (Section 4), and in particular to probe how AGN feedback comes into play, an additional catalogue is used: $\mathscr{C}_{\text{Hzagn 3D}}$, built from the HORIZON-AGN snapshot outputs.[3] The simulation is described in the following section, and a summary of all the catalogues used in this study is presented in Table 1.

2.2.1 Description of the simulation

The HORIZON-AGN simulation run has been performed with RAM-SES, an adaptive mesh refinement code introduced by Teyssier (2002). The size of the simulation box is $L_{\text{box}} = 100\,h^{-1}$ Mpc on

a side, and the volume contains 1024^3 dark matter (DM) particles (which corresponds to a DM mass resolution of $M_{\text{DM,res}} = 8 \times 10^7\,M_\odot$). The initial grid is adaptively refined down to 1 physical kpc, leading to a typical number of 6.5×10^9 leaf cells at $z = 1$. The refinement is triggered when the number of DM particles becomes greater than eight or the total baryonic mass reaches eight times the initial DM mass resolution in a cell.

A uniform UV background is switched on at $z_{\text{reion}} = 10$ following Haardt & Madau (1996). Gas cools down to 10^4 K via H, He, and metals (following Sutherland & Dopita 1993). Star particles are created in regions where gas number density is above $n_0 = 0.1\,\text{H cm}^{-3}$, following a Schmidt law: $\dot{\rho}_* = \epsilon_* \rho_g/t_{\text{ff}}$, where $\dot{\rho}_*$ is the star formation rate mass density, ρ_g the gas mass density, $\epsilon_* = 0.02$ the constant star formation efficiency, and t_{ff} the gas local free-fall time. A subgrid model for feedback from stellar winds and supernova (both type Ia and II) is implemented with mass, energy, and metal releases in the surrounding gas. HORIZON-AGN also follows galactic black hole formation, with black hole energy release in either quasar or radio mode depending on the accretion rate (see Dubois et al. 2012, for more details).

Out of the entire HORIZON suite, we mostly use the HORIZON-AGN simulation in this paper. However, we will briefly compare it to its identical twin without AGN feedback, HORIZON-NOAGN (Peirani et al. 2017), to highlight the impact of such a feedback on the properties of BGGs. Overall, the stellar mass build-up of galaxies in HORIZON-AGN is found in good agreement with observations. As shown in Kaviraj et al. (2017), the stellar-mass and luminosity functions agree reasonably with observational data across the redshift range $0 < z < 4$. This agreement is obtained at the high-mass end due to the inclusion of AGN feedback in the simulation. The main remaining point of tension is that HORIZON-AGN tends to overestimate galaxy masses below the knee of the luminosity function at all epochs. This does not affect our analysis however, since we focus only on the most massive galaxies (BGG masses are higher than $\sim 10^{10.5}\,M_\odot$).

2.2.2 The snapshot catalogue: $\mathscr{C}_{\text{Hzagn 3D}}$

In order to identify galaxies from the stellar particles distribution, we run the ADAPTAHOP halo finder (Aubert, Pichon & Colombi 2004) on the snapshots. Local stellar particle density is computed from the 20 nearest neighbours, and we keep in the catalogue galaxies with a density threshold equal to 178 times the average matter density at that redshift.

We then extract DM haloes from the DM particle distribution following the same procedure as for galaxies, but with a density threshold of 80 times the average matter density. Only haloes with

---

[2]http://www.horizon-simulation.org/
[3]The reason why snapshot outputs are used here (instead of the light-cone) is to increase the statistics

more than 100 particles are kept in the catalogue. The centre of the halo is temporarily defined as the densest particle in the halo, and then refined with the shrinking sphere method (Power et al. 2003) in order to recursively find the centre of mass of the halo.

Each galaxy is associated with its closest main halo, and to match the observational definition, the BGG is identified as the most massive galaxy within the virial radius of the main halo. In order to increase the statistics, this group catalogue (called $\mathscr{C}_{\text{Hzagn 3D}}$ in the following) is built by joining the data from three snapshot outputs at $z = 0.63$, 0.81, 1.03.[4] This results in 1115 groups with $M_{\text{group}} > 10^{13}\,\text{M}_\odot$. In order to get the quenching efficiency for the BGG (Section 4), the galaxy catalogue is matched with its counterpart in the HORIZON-NOAGN simulation $\mathscr{C}_{\text{Hznoagn 3D}}$. The matching procedure is fully described in Peirani et al. (2017) and Beckmann et al. (2017). The matching procedure identifies 876 groups of $\mathscr{C}_{\text{Hzagn 3D}}$ which have a counterpart in $\mathscr{C}_{\text{Hznoagn 3D}}$. For these groups, the quenching efficiency due to AGN feedback is defined for matched galaxies as: $\xi = \log(M_{*\,\text{Hz−noAGN}}/M_{*\,\text{Hz−AGN}})$. This quenching efficiency is therefore zero when the galaxy mass is the same in HORIZON-AGN and HORIZON-NOAGN.

TREEMAKER (Tweed et al. 2009) is used to build merger trees from the halo catalogues. Each halo in a given snapshot at a given redshift is connected to its main progenitors at higher redshift and its child at lower redshift. Merger trees are built over 38 snapshots in the redshift range $z = [0.63, 5.87]$ corresponding to a time step of about ∼200 Myr. For each group, we look at its merger history by following back in time its merger tree. The halo is assumed to have encountered a major merger of ratio greater than (1:x) if the mass ratio of the second to the main progenitors is greater than $1/x$.

2.2.3 The light-cone catalogues: $\mathscr{C}_{\text{Hzagn 2D}}^{\text{true}}$ and $\mathscr{C}_{\text{Hzagn 2D}}^{\text{phot}}$

The HORIZON-AGN light-cone has been extracted on-the-fly as described in Pichon et al. (2010). Gas cells have been replaced by gas particles, and treated as stars and DM particles. The light-cone projected area is 5 deg^2 below $z = 1$, and 1 deg^2 above. ADAPTAHOP has been run on the light-cone over the redshift range $0 < z < 4$ with the same method as described above. Photometry is computed for each galaxy in the same filter passbands as those available in the COSMOS2015 catalogue, as fully described in Laigle et al. (2019). We simply recall here the main features of this catalogue. For a given galaxy, each of its stellar particles is linked to a single stellar population (SSP) obtained with the stellar population synthesis model of Bruzual & Charlot (2003), with a Chabrier initial mass function (IMF, Chabrier 2003). The galaxy spectrum is the sum of the contributions of the individual SSP. Dust attenuation is also accounted for. From this virtual photometry, photometric redshifts and masses have been derived with LEPHARE (Arnouts et al. 2002) with the same configuration as in COSMOS, and the performance of the simulated catalogue is very similar to the observed one in terms of redshift and mass accuracy (Laigle et al. 2019). $\mathscr{C}_{\text{Hzagn 2D}}^{\text{true}}$ is the catalogue which uses the exact galaxy redshifts and masses, while $\mathscr{C}_{\text{Hzagn 2D}}^{\text{photo}}$ uses the photometric redshifts and masses. In order to mimic COSMOS data, we keep only groups more massive than $10^{13.3}\,\text{M}_\odot$ and containing a BGG more massive than $10^{10}\,\text{M}_\odot$. We are left with 76 groups over 1 deg^2, which is slightly more than in COSMOS. However cosmic variance is expected to be quite important on these small fields, and the COSMOS group density

should be corrected for the small variation of the group mass limit to be fully comparable to the simulated group density.

2.3 Extraction of filaments and connectivity estimator

2.3.1 Extraction of the filaments in 3D

To identify the cosmic network from the density field, we use the persistence-based filament tracing algorithm (DISPERSE, Sousbie 2011), which identifies ridges from the density field as the special lines connecting topologically robust pairs of saddle-peak critical points. Therefore, the extraction is global in the sense that what determines the presence of a filament at a given location is not only the amplitude of the overdensity with respect to the local background, but also the distribution of matter on a larger scale (i.e. the presence of a saddle point or a peak further away). In the following, we call 'nodes' the maxima of the density field (where filaments are crossing). In Sousbie, Pichon & Kawahara (2011), DISPERSE was successfully used to extract filaments around an X-ray-detected group at $z = 0.083$. For the 3D extraction of the filaments in HORIZON-AGN, the density field is reconstructed from the Delaunay tessellation on the entire sample of DM haloes (Schaap & van de Weygaert 2000).

Each filament is defined as a set of connected small segments linking extrema to saddle points. The set of filaments is called the skeleton in the following. Persistence is defined as the difference in density at the two critical points within a pair. Expressed in terms of numbers of σ, persistence quantifies the significance of the critical pairs in the Delaunay tessellation of a random discrete Poisson distribution. Thus, the filtering of low-persistence structures ensures that the extraction is robust with respect to noise. We choose a 5σ persistence threshold to extract filaments in 3D from HORIZON-AGN.

2.3.2 Extraction of the filaments in 2D

For the observed catalogue ($\mathscr{C}_{\text{cosmos}}$) and the simulated ones from the light-cone ($\mathscr{C}_{\text{Hzagn 2D}}^{\text{true}}$ and $\mathscr{C}_{\text{Hzagn 2D}}^{\text{phot}}$), filaments of the cosmic web are identified from the 2D density field, computed from the Delaunay tessellation of the galaxy distribution, following Laigle et al. (2018). However, we introduce two changes compared to this previous extraction.

Choice of the slice thickness: We consider slices of a fixed comoving thickness 120 Mpc instead of 75 Mpc (as was chosen in Laigle et al. 2018). The motivation is to increase the redshift range of the study (up to $z \sim 1.2$ instead of $z \sim 0.9$) while keeping the thickness of the slices calibrated on the typical redshift uncertainty of the lowest mass galaxies in our mass-limited sample ($\Delta_z \sim 0.07$, that is about 120 cMpc, at $z \sim 1.2$ for $\log M_*/\text{M}_\odot \sim 10$). As shown in Laigle et al. (2018), there is no truly optimal slice thickness for extracting filaments (within some range), allowing for a flexible choice without degrading the quality of the extraction. It should in practice primarily be guided by the photometric redshift uncertainties of the lowest mass galaxies in the sample. More specifically, the slice thickness is taken as two times the σ_z uncertainty[5] of the 5000 lowest mass galaxies in the redshift and mass bin considered. In order to get a constant slice thickness over the whole redshift range, we calibrate the slice thickness on the

---

[4]which ultimately is a procedure similar to the building of a very low-resolution light-cone.

[5]σ_z is defined for each galaxy and encompasses 68 per cent of the PDF(z) around the median redshift.
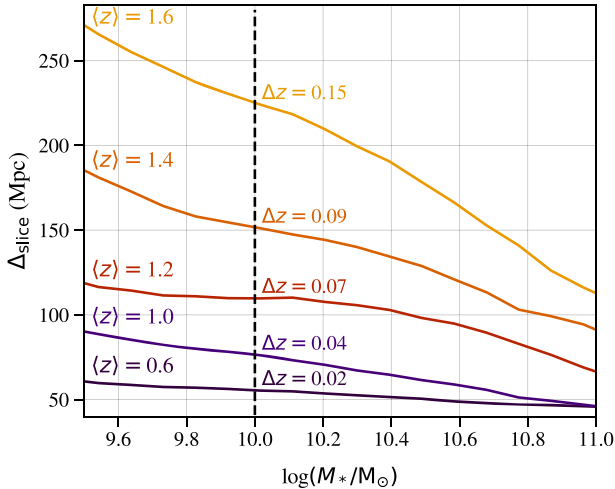
Figure 2. Minimal slice thickness Δ_{slice} in comoving Mpc which has to be chosen in $\mathscr{C}_{\text{cosmos}}$ for the purpose of cosmic web extraction in 2D, as a function of masses and for different redshifts (from $\langle z \rangle = 1.6$ to $\langle z \rangle = 0.6$, yellow to dark blue lines). Here Δ_{slice} is the comoving thickness corresponding to $\Delta z = 2 \times 1\sigma_z$, where σ_z is the redshift uncertainty of the lowest mass galaxies in the sample. Above each line is also indicated Δz corresponding to the galaxies in the $10^{10} \, \text{M}_\odot$ bin.

lowest mass galaxies at $z \sim 1.2$. As shown in Fig. 2, this implies considering slices of thickness ~ 120 comoving Mpc. Note that the slice thickness should also be larger than the velocity dispersion in large groups ($\sim 1000 \, \text{km s}^{-1}$), which is still small in Δ_z compared to the adopted thickness slices.

The second major change with respect to the analysis in Laigle et al. (2018) concerns the centring of the slices. Because our study is focused on the extraction of filaments around groups, we perform an individual extraction of the filaments for all the groups in our catalogue, each of the groups being put at the centre of its own slice. This requirement ensures an optimal extraction of the filaments around all the groups.

Choice of the persistence threshold in 2D: Laigle et al. (2018) chose a persistence threshold of 2σ for slice thickness of 75 Mpc at the same mass completeness as ours. This choice was justified by comparing in mocks the 2D photometric skeleton with the projected 3D one. As shown in their Fig. A1, minimizing the number of unmatched filaments in the reference and in the reconstructed skeletons implies decreasing the persistence threshold with increasing slice thickness (at a given mass completeness). Therefore, we use in this work a persistence threshold of 1.5σ.[6]

2.3.3 Method to measure the connectivity

In the skeleton produced by DISPERSE, two filaments joining the same node can become extremely close to one another, but still counted separately, as they both are topologically robust. However, physically they represent a single filament. Therefore, in order

to avoid double counting filaments, they are merged in the final skeleton and a bifurcation point is added at the merging location.[7]

The same ID is then attributed to all segments belonging to the same filaments. Connectivity $\mathcal{C}$ is subsequently defined as the number of segments with different IDs crossing the 1.5 times virial radius circle around the group centre. The same definition is taken in 3D and 2D. In Appendix A we confirm on the observational data set that varying this radius does not significantly change the measurement of connectivity and the signal presented hereafter.

Fig. 3 presents six groups in the COSMOS field, with varying masses, redshifts, and connectivity, plotted over the underlying density field estimated from the Delaunay tessellation. Distinct filaments are shown in different colours. The BGG is coloured in red, while the other galaxies in the group are coloured in white. On all these panels, the groups are associated with a peak of the galaxy density distribution, i.e. they are sitting on a node of the cosmic web. The *bottom right* panel is an example of the highest connectivity found ($4 - \mathcal{C}$, i.e. the group is connected to four filaments), while the bottom left panel shows an example of the lowest connectivity found that is still associated with a peak in the distribution ($1 - \mathcal{C}$, i.e. the group is connected to only one filament). While a $1 - \mathcal{C}$ connectivity is unlikely to happen in theory, this case is found in observations because low-persistence filaments were removed from the skeleton. Therefore this group is connected to more filaments, however all but one were too noisy to pass the persistence threshold selection.

2.4 Impact of photo-*z* errors: insights from mocks

The degradation of the global filament extraction when working with photo-*z* has already been investigated in Laigle et al. (2018). However we focus here on the degradation of the 2D-connectivity measurement, due to the comparison of $\mathscr{C}^{\text{phot}}_{\text{Hzagn 2D}}$ and $\mathscr{C}^{\text{true}}_{\text{Hzagn 2D}}$. The grey histograms on the top and middle panels of Fig. 4 present the PDF of group connectivity from the HORIZON-AGN simulation, either using the true galaxy redshift (*panel A*, $\mathscr{C}^{\text{true}}_{\text{Hzagn 2D}}$) or the photo-*z* (*panel B*, $\mathscr{C}^{\text{phot}}_{\text{Hzagn 2D}}$) to extract the 2D cosmic web. The vertical solid black lines give the mean of each distribution. Photo-*z* errors tend to decrease the global connectivity, as they introduce shot noise in the density measurement and therefore disconnect the field.

In practice, when the measure is performed from photo-*z* ($\mathscr{C}_{\text{cosmos}}$ and $\mathscr{C}^{\text{phot}}_{\text{Hzagn 2D}}$), a non-negligible number of groups are found which are not connected to filaments. Another non-negligible number of groups are embedded in filaments but not associated with a peak of the galaxy density distribution above the persistence threshold ($1a - \mathcal{C}$). Finally, others are associated with a peak of the galaxy distribution, but associated to only one filament ($1b - \mathcal{C}$), because the other filaments have been removed when filtering the pairs of critical points below the persistence threshold. These cases are unlikely to occur when connectivity is computed from true galaxy redshifts and are mostly due to noise in the photo-*z*. Indeed, their fractions is almost null in $\mathscr{C}^{\text{true}}_{\text{Hzagn 2D}}$ (*top* panel), and in particular no $1a - \mathcal{C}$ case is found.[8]

---

[6] In addition, a persistence of 1.5σ allows to optimally recover the filaments in the mocks ($\mathscr{C}^{\text{phot}}_{\text{Hzagn 2D}}$) with respect to the intrinsic distribution ($\mathscr{C}^{\text{true}}_{\text{Hzagn 2D}}$). A 2σ persistence however underestimates the connectivity in the mocks $\mathscr{C}^{\text{phot}}_{\text{Hzagn 2D}}$, especially for highly connected groups. A 1.5σ persistence allows to mitigate this underestimation.

[7] In this sense, we measure multiplicity and not connectivity, in the wording of Codis et al. (2018).

[8] To confirm that these situations are created by photo-*z* uncertainties and are not driven by some physical properties of these groups, we compare the distributions of group mass and BGG mass for the low connectivity sample ($0 - \mathcal{C}$, $1a - \mathcal{C}$, and $1b - \mathcal{C}$) with the ones for the high connectivity
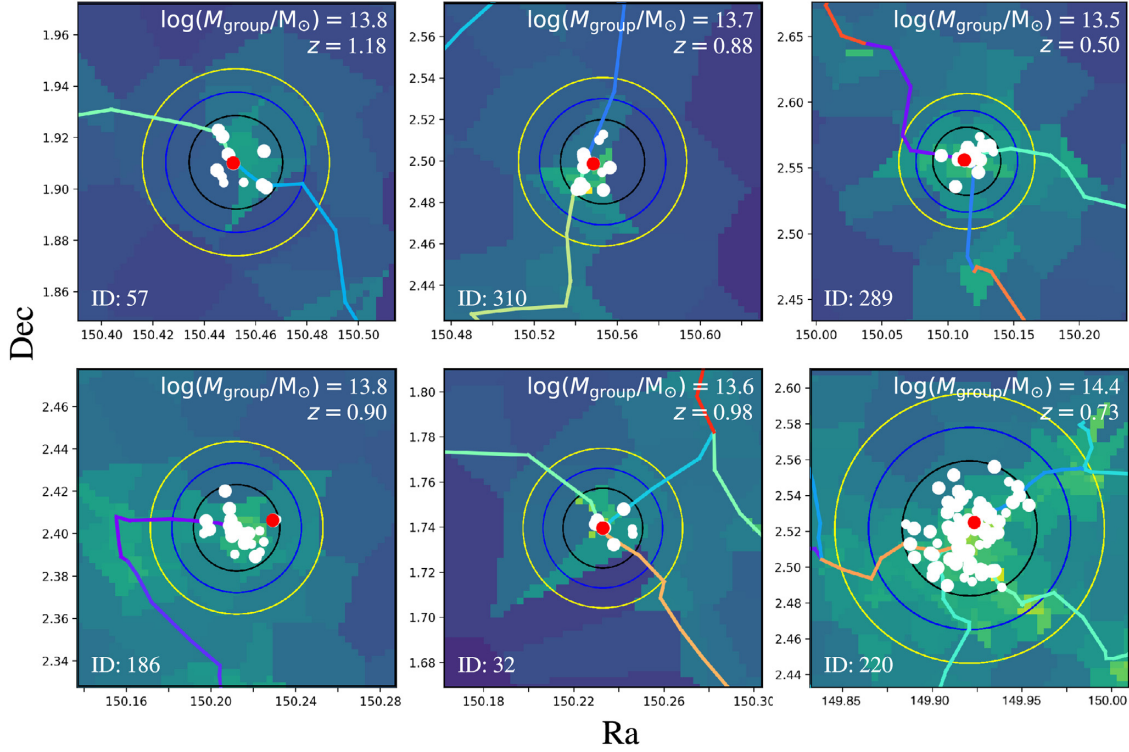
Figure 3. Example of the connectivity of groups of different masses at different redshifts in $\mathscr{C}_{\text{cosmos}}$. Each panel is 4 comoving Mpc wide, and the *x*- and *y*-axis indicate, respectively, right ascension and declination. The black, blue, and yellow circles are drawn, respectively, at 1, 1.5, and 2 times the virial radius of the group. The connectivity at a given radius is defined as the number of filaments crossing the corresponding circle. Galaxies are represented by white discs. The large and small discs correspond to galaxies more massive and less massive than 10^{10} $M_{\odot}$, respectively. Only galaxies identified as members of the group and with $\log M_*/M_{\odot} > 9.5$ are shown. The BGG is in red. Distinct filaments have different colours. The background density is estimated from the Delaunay tessellation.

It is debatable if groups embedded in filaments but not associated with a peak of the density distribution ($1a-\mathcal{C}$) should be counted as $1-\mathcal{C}$ or $2-\mathcal{C}$, as there are formally two filaments branching out of these groups. The comparative analysis from the detailed mocks suggests these groups should sit at a density peak in the absence of photo-*z* errors. Therefore in the following we make the choice to consider them as $2-\mathcal{C}$ (*grey* histograms on Fig. 4) instead of $1-\mathcal{C}$ (*pink* histograms). Appendix A2 discusses this issue in more details. For each measurement based on $\mathscr{C}_{\text{cosmos}}$ presented in the following, we also checked that the result is not strongly dependent on this choice.

3 GROUP CONNECTIVITY IN COSMOS

The *grey* histograms on the *middle* and *bottom* panels of Fig. 4 show the distribution of the connectivity in the full redshift range $0.5 < z < 1.2$ in the HORIZON-AGN and COSMOS data sets. We measure $\langle \mathcal{C} \rangle = 2.02$; RMS $(\mathcal{C}) = 0.92$ in $\mathscr{C}_{\text{cosmos}}$, $\langle \mathcal{C} \rangle = 2.56$; RMS $(\mathcal{C}) = 1.10$ in $\mathscr{C}_{\text{Hzagn 2D}}^{\text{true}}$ and $\langle \mathcal{C} \rangle = 1.89$; RMS $(\mathcal{C}) = 1.18$ in $\mathscr{C}_{\text{Hzagn 2D}}^{\text{phot}}$.

3.1 Mean connectivity and group mass dependency

The mean group connectivity as a function of group mass can now be measured. In both COSMOS and the HORIZON-AGN data sets,

sample ($1 < \mathcal{C}$). We do not observe any significant bimodality between the distributions of both samples, the low-$\mathcal{C}$ sample behaving like the low-mass tail of the high-$\mathcal{C}$ one.

the group mass M_{group} is defined as the total mass, i.e. the sum of DM and baryonic mass. The left-hand panel of Fig. 5 displays this measurement in the mock ($\mathscr{C}_{\text{Hzagn 2D}}^{\text{phot}}$ and $\mathscr{C}_{\text{Hzagn 2D}}^{\text{true}}$, *green* solid and dashed lines resp.) and in COSMOS ($\mathscr{C}_{\text{cosmos}}$, *black* line). Group mass bins are split to contain an approximately equivalent number of groups in each bin. Unsurprisingly and as discussed above, the measurement performed with true-*z* lies above the one with photo-*z*. The COSMOS and photo-*z* HORIZON-AGN data sets are however in very good agreement. As expected from theoretical predictions (Codis et al. 2018), more massive groups have, on average, a higher connectivity.

3.2 Impact of connectivity on BGG mass assembly

The impact of the connectivity on the mass assembly of the BGG is now investigated. Our purpose is to quantify if there is any correlation between connectivity and the BGG properties (mass and type) beyond the trend driven by the group mass (which scales with connectivity). The adopted strategy is therefore to look at each of these quantities in bins of group mass.

3.2.1 Mass of the BGG

The overall evolution of mean connectivity as a function of BGG mass is first measured. This result is displayed in the right-hand panel of Fig. 5. As a consequence of the assumptions made at the SED-fitting stage when computing masses from photometry (Laigle et al. 2019), the BGG photometric masses are systematically
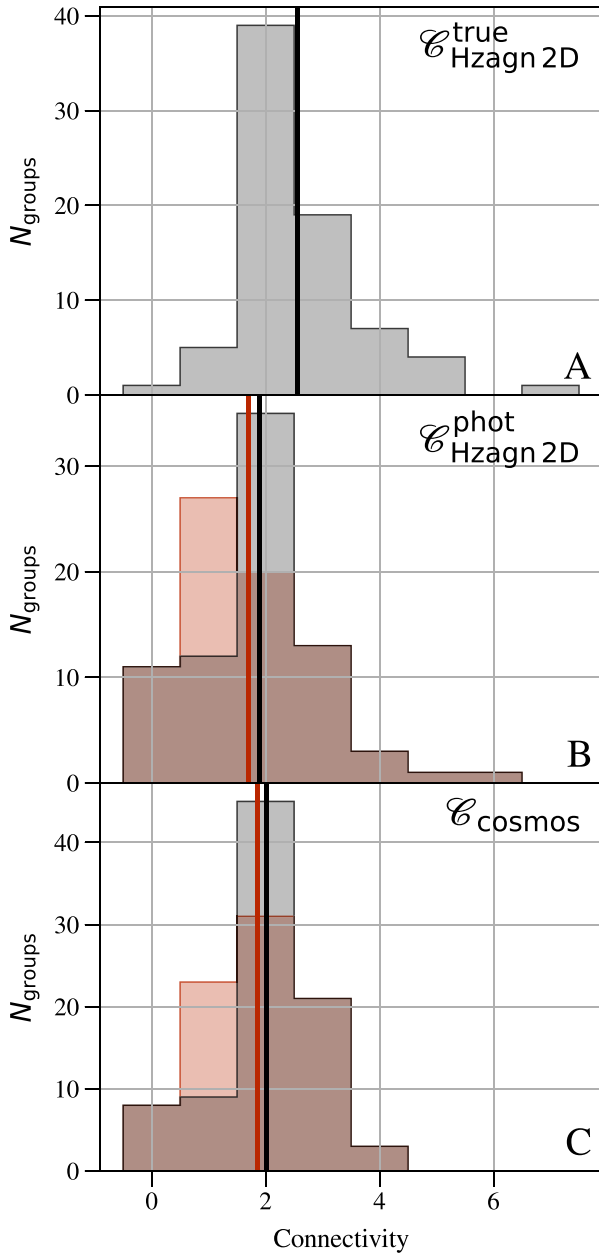
Figure 4. Distribution of group connectivity using a filament extraction based on true-z (*panel A*) and photo-z (*panel B*) from the HORIZON-AGN simulation. The *panel C* shows the PDF of the connectivity in the COSMOS data set. The *grey* and *pink* histograms correspond to the distribution with $1a - \mathcal{C}$ groups classed as $2-\mathcal{C}$ or $1-\mathcal{C}$, respectively (see the text for details). The *black* and *red* lines correspond to the mean of the *grey* and *pink* histograms, respectively.

underestimated with respect to their intrinsic mass in HORIZON-AGN, which is the reason for the horizontal offset between the *solid* and *dashed green* curves. Taking into account this systematic, as well as the lowering of the connectivity when computed from photometric redshifts, brings $\mathcal{C}^{\mathrm{phot}}_{\mathrm{Hzagn\,2D}}$ in good agreement with $\mathcal{C}_{\mathrm{cosmos}}$ within the errorbars (*green* and *black* curves, respectively). As expected, the connectivity is higher when the BGG is more massive. At first order this result is a natural consequence of the scaling of group mass with connectivity. Indeed, in a now well-established feature of our galaxy formation model, the galaxy stellar

mass assembly primarily depends on the mass assembly of their host DM haloes. One of the most straightforward consequence of this dependency is the stellar-to-halo mass relationship, which has been now extensively measured and studied up to high redshift (e.g. Zaritsky & White 1994; Berlind & Weinberg 2002; Bullock, Wechsler & Somerville 2002; Cooray & Sheth 2002; Vale & Ostriker 2004; Behroozi, Conroy & Wechsler 2010; Reddick et al. 2013; Legrand et al. 2019, and references therein). This relation still hold for massive objects, and in particular shall hold for the groups considered in this study, provided that our total group masses computed from X-ray luminosity are a good representation of the dark matter halo masses (see e.g. Eckmiller, Hudson & Reiprich 2011, for a discussion on the robustness of computing group masses from X-ray).

In order to investigate if there is an additional correlation between connectivity and BGG mass (beyond the effect driven by group mass), the *top* panel of Fig. 6 presents the BGG mass as a function of group mass in three different connectivity bins. The *bottom* panel presents how groups are distributed within the mass and connectivity bins. Group mass bin are uniformly distributed in logarithm scale between $10^{13.38}$ and $10^{14.02}\,\mathrm{M_\odot}$. At fixed group mass in the low-mass bins ($M_{\mathrm{group}} \lesssim 10^{13.7}\,\mathrm{M_\odot}$), there is a significant trend for the BGG to have higher mass at higher connectivity. In the highest mass bins, the mass of the BGG for groups with $\mathcal{C} \geq 3$ (*yellow solid* line) is on average lower as those with $\mathcal{C} = 2$ (*red* line). Note that two groups in the highest connectivity bin have their mass higher than $10^{14}\,\mathrm{M_\odot}$, and are therefore not included by default on the highest mass bin. Including them (*yellow triangle* marker) in the highest mass bin sensibly biases the mass distribution of groups in this connectivity bin (compared to the medium connectivity bin). In spite of this, the mean BGG mass is still lower than the one in the medium connectivity bin (compare the last *red circle* marker and the *yellow triangle* marker). We also checked that this measurement is not strongly dependent on the choice we made to consider $1a-\mathcal{C}$ groups as $2-\mathcal{C}$ (compare *solid* and *dashed* lines).

Although this result needs more statistics to be confirmed, it suggests that low-mass groups build more efficiently the mass of their BGG at high connectivity, while in high-mass group there is a stagnation of the BGG mass assembly at high connectivity. Altogether, this suggests that connectivity might trace different assembly histories of groups.

3.2.2 Type of the BGG

To further probe the link between connectivity and the mass assembly of the BGG, the relationship between connectivity and group mass is investigated in COSMOS by splitting the group population as a function of the type of their BGG. The classification between star-forming and passive galaxies is performed according to the $M_{\mathrm{NUV}} - M_{\mathrm{r}}/M_{\mathrm{r}} - M_{\mathrm{J}}$ diagram as shown in the left-hand panel of Fig. 7 (as done in Williams et al. 2009; Ilbert et al. 2013; Laigle et al. 2016). Quiescent galaxies are those with $[M_{\mathrm{NUV}} - M_{\mathrm{r}} > 3(M_{\mathrm{r}} - M_{\mathrm{J}}) + 1]$ and $[M_{\mathrm{NUV}} - M_{\mathrm{r}} > 3.1]$. Most of the BGG are passive, however 13 of them are classified as star-forming, with group mass ranging from $10^{13.41}$ to $10^{13.89}\,\mathrm{M_\odot}$. In this mass range, the mean connectivity of groups with a passive BGG is $\langle \mathcal{C}_{\mathrm{pass}} \rangle = 2.09$, while it is $\langle \mathcal{C}_{\mathrm{sf}} \rangle = 1.3$ for the groups with a star-forming BGG. In the left-hand panel of Fig. 7, circles representing BGG are colour-coded according to the connectivity of their group, and their size scales with the mass of the group. Although some groups with a passive BGG have a low connectivity, no star-forming
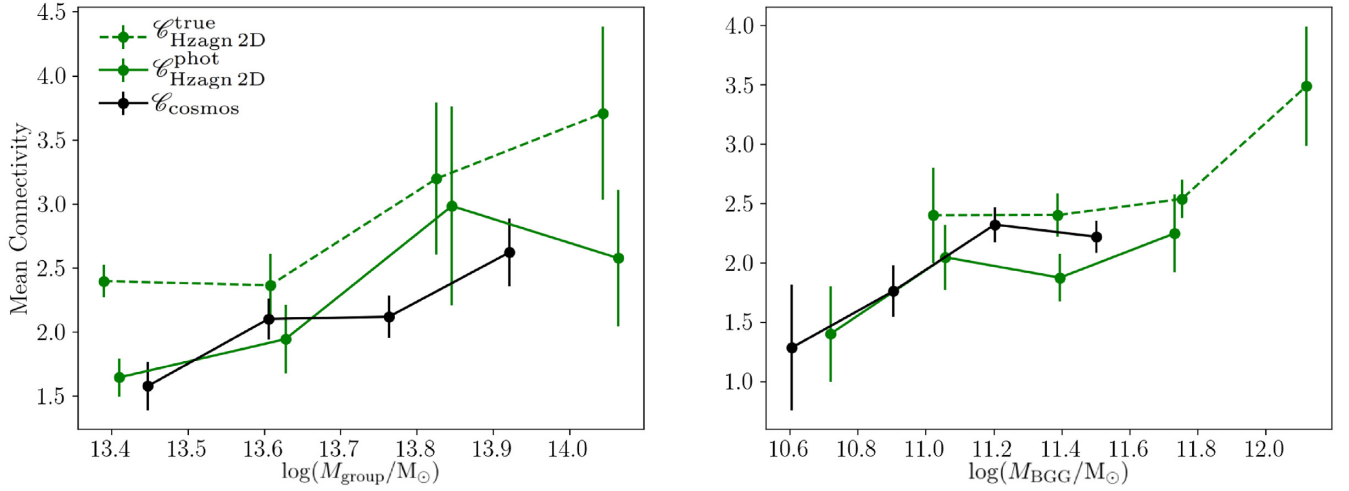
Figure 5. Mean connectivity plotted against group mass M_{group} (*left*) and BGG mass M_{BGG} (*right*) for COSMOS data (*black* line) and the Horizon-AGN simulation (*green* line) for both photo-z (*solid* line) and true-z (*dashed* line) filament extractions. Photometric masses are also used to compute the relation between mean connectivity and BGG mass in the HORIZON-AGN mock data set, which is the reason for the horizontal offset between the *solid* and *dashed* curves on the right-hand panel. Errorbars are the error on the mean computed from bootstrap resampling.
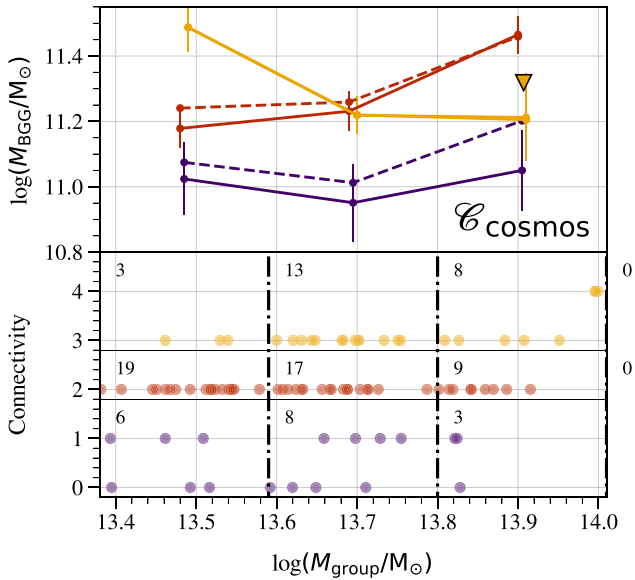
Figure 6. The BGG mass against group mass for groups with connectivity smaller than two (*blue* line), connectivity of two (*red* line) and connectivity greater than two (*yellow* line). Two groups of connectivity greater than two have their mass higher than 10^{14} M$_\odot$. When they are included in the measurement of the last mass bin, we get the *yellow triangle* marker. The dashed lines correspond to the same measurements, but when classifying the 1a−$\mathcal{C}$ as 1−$\mathcal{C}$ instead of 2−$\mathcal{C}$. The *bottom* panel shows the distribution of groups in bins of connectivity and group mass. In the corner of each 2D bin is indicated the number of groups in this bin.

BGG except one (in the vicinity of the separation line) are in the highest connectivity bin.

As a complement, the right-hand panel of Fig. 7 presents the mean connectivity, as a function of group mass, of groups with either a passive or a star-forming BGG. At a fixed group mass, the mean connectivity of groups with a passive BGG is higher than for groups with a star-forming BGG. This result suggests that higher

connectivity implies a higher chance for the BGG to be quenched. The analysis of the HORIZON-AGN simulation in Section 4 will help interpret this result.

4 INTERPRETATION AND DISCUSSION

4.1 Summary of the observational findings

The observational results presented in the previous section confirm first that connectivity scales as a function of group mass. The agreement of this result with theoretical predictions is also indirectly a quality assessment of the filament extraction from photo-z redshift in COSMOS. The relation between BGG mass and connectivity is at first order a natural consequence of the relation between group mass and connectivity.

We also investigated the correlation between connectivity and the properties of the BGG (mass and type) beyond the trend which could be deduced from the correlation between connectivity and group mass. We found that, in low-mass groups ($M_{group} \lesssim 10^{13.7}$ M$_\odot$), the mass of the BGG is on average higher if the connectivity is higher. This trend reverses above this mass, with BGGs in highly connected groups ($\mathcal{C} \geq 3$) being on average less massive than their counterparts in groups of the same mass (Fig. 6). In addition, even if passive galaxies are found both at low and high connectivity, BGGs hosted by highly connected groups are always passive (Fig. 7), suggesting a quenching process connected with (but not necessarily caused by) a high connectivity.

Several physical processes might be responsible for this trend. First, assuming gas accretion rate scales with connectivity, one can expect that higher gas infall along more filaments triggers stronger feedback within the BGG. This feedback could in turn prevent stellar mass growth. This interpretation is appealing, as it could both explain the trend at low group mass (higher connectivity groups host more massive galaxies, because more matter is efficiently accreted on to the BGG) and the reverse of this trend at high group mass (the higher accretion rate in high connectivity triggers stronger AGN feedback). These findings might also be an outcome of assembly bias, in which higher connectivity might be a tracer of recent group
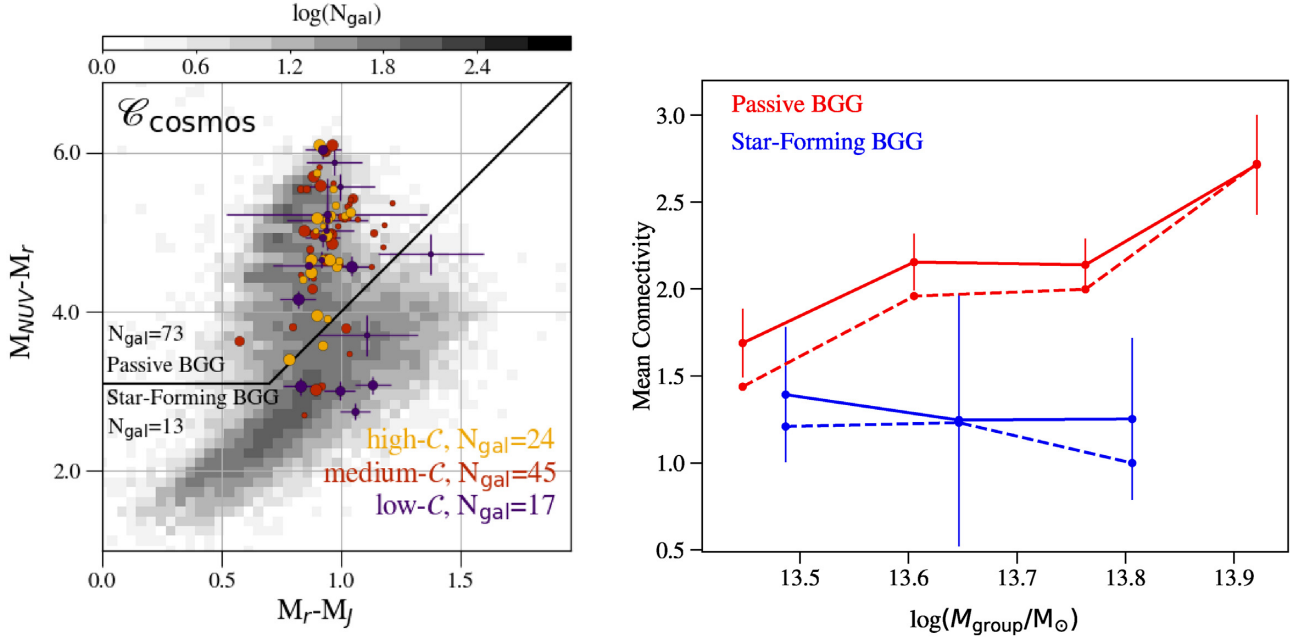
Figure 7. *Left*: $M_{\mathrm{NUV}} - M_{\mathrm{r}}/M_{\mathrm{r}} - M_{\mathrm{J}}$ distribution for the entire galaxy population in $0.5 < z < 1.2$ and $M_* > 10^{10}\,\mathrm{M}_\odot$ in COSMOS (*grey* area), and for the BGGs only in the same redshift and mass ranges (coloured circles). The circles are coloured according to their connectivity (from low to high connectivity, *blue* to *yellow*, respectively, according to the binning shown in Fig. 6), and their sizes reflect the group masses. The solid line is the usual separation between passive and star-forming galaxies (see the text). For clarity, only errorbars for the low-connectivity BGGs are shown. *Right*: Mean connectivity as a function of group mass in COSMOS, for groups with a passive BGG (*red* line) and groups with a star-forming one (*blue* line). The dashed lines correspond to the same measurements, but when classifying the $1a - \mathcal{C}$ groups as $1 - \mathcal{C}$ instead of $2 - \mathcal{C}$.

mergers. As a matter of fact, when two groups of connectivity n and m, respectively, are merging along a filament, their other filaments are likely to not merge in the same time-scale. The net connectivity resulting of the merger will therefore be $n + m - 2$. As long as both n and m are greater than two, the resulting connectivity will be higher than the mean connectivity of the two progenitors. Mergers are violent events. The merger of two haloes – and consequently their two central galaxies – might shock-heat the gas, but also increase the velocity dispersion, enhance black hole growth, and in particular be the reason for stronger AGN feedback (e.g. Di Matteo, Springel & Hernquist 2005). Although mergers can temporarily trigger bursts of star formation (e.g. Di Matteo et al. 2007; Martin et al. 2017), the merger-enhanced AGN activity can in the long-term durably quench the galaxies (e.g. Springel, Di Matteo & Hernquist 2005; Dubois et al. 2016). This interpretation from mergers is consistent with previous works finding that SFR is enhanced in isolated groups compared to groups embedded in larger structures (e.g. Scudder et al. 2012, where AGN however have been explicitly excluded from the sample; Luparello et al. 2015).

4.2 Interpretation from HORIZON-AGN

We also conduct complementary measurements in the HORIZON-AGN simulation with the $\mathcal{C}_{\mathrm{Hzagn\,3D}}$ catalogue in order to understand the observational results.

Mean connectivity is first measured as a function of group mass both for groups with a passive and star-forming BGG. Separating passive and star-forming BGGs from the $M_{\mathrm{NUV}} - M_{\mathrm{r}}/M_{\mathrm{r}} - M_{\mathrm{J}}$ diagram is less easy in HORIZON-AGN than in COSMOS, as there is residual star formation even in the passive systems (Kaviraj et al. 2017). For this reason we decided to sort galaxies based on their

specific star formation rate (sSFR) and to define the star-forming sequence as the galaxies with the highest sSFR and the passive sequence as the galaxies with the lowest sSFR (note that the trend does not change when galaxies are sorted according to their SFR rather than their sSFR). Fig. 8 shows the mean connectivity as a function of group mass in $\mathcal{C}_{\mathrm{Hzagn\,3D}}$ (*solid* line), for the groups with a passive (*red* lines) and star-forming (*blue* lines) BGG, while choosing two extreme thresholds (in percentage of the total population) to separate the star-forming from the passive BGGs. Overall, whatever the chosen threshold, a trend qualitatively similar to the observations is found in the simulation: the mean connectivity of groups with a star-forming BGG is lower than the one with a passive BGG, especially at high group mass. However, we note that the typical group mass for which a difference between the mean connectivity of the star-forming and passive populations is measurable ($\log M_{\mathrm{group}} > 10^{13.8}\,\mathrm{M}_\odot$) is higher than in $\mathcal{C}_{\mathrm{cosmos}}$ ($\log M_{\mathrm{group}} > 10^{13.5}\,\mathrm{M}_\odot$). We carry out the same measurement in the simulation without AGN feedback (*dashed* line) and a weaker trend emerges, suggesting that AGN feedback is important to durably quench the galaxies at high connectivity, but might not be the only driver of the trend.

We turn then to measuring the mean BGG mass as a function of group mass, in bins of connectivity (*panel A* of Fig. 9). As found in observations, the high-mass groups in the highest connectivity bins tend to have a lower mean BGG mass than those in the intermediate connectivity bins, although the trend is not very significant. We do not find a significant reversal of this trend at low group mass (the fact that more connected groups have a more massive BGG at fixed group mass).

In order to understand the role AGN feedback plays in driving this trend, the mean quenching efficiency due to AGN feedback is
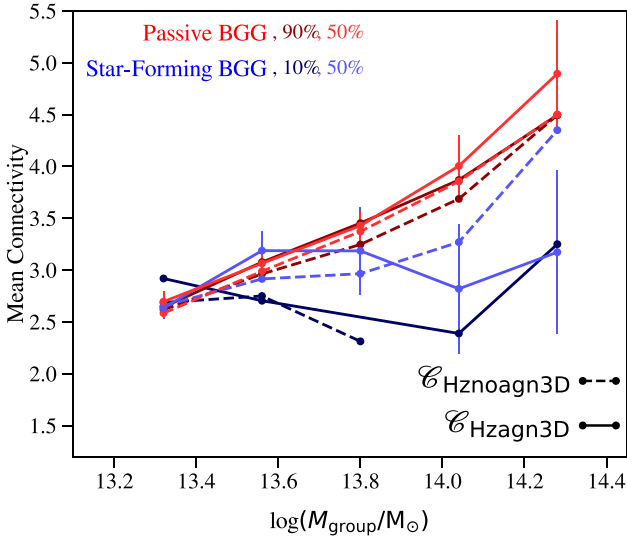
Figure 8. Mean connectivity as a function of group mass in the HORIZON-AGN (*solid* line) and HORIZON-NOAGN (*dashed* line) for passive (*red*) and star-forming (*blue*) BGGs, while chosing the two extreme thresholds (from dark to light colours) to separate the passive population from the star-forming one (see the text for details). For clarity, only errorbars on the lightest curves are shown.

also displayed as a function of group mass, in distinct connectivity bins. A strong signal for quenching efficiency to be higher in high connectivity groups is detected (*panel B* of Fig. 9).

We then measure, in each connectivity bin, the fraction of groups with a recent major merger of ratio greater than (1:2) (*panel C* of Fig. 9). There is a significant signal for this fraction to be higher at higher connectivity. Finally, we measure in bins of group mass the average time spent since the last major merger with a mass ratio greater than (1:3) (*panel D* of Fig. 9). At a given group mass, there is a significant signal for the haloes in the highest connectivity bin to have encountered a major merger more recently than in the lower connectivity bins.

Consistently with the observational results at high group mass, our measurements support a scenario in which high connectivity is associated with a stagnation of star formation. In addition, we found higher AGN quenching efficiency at higher connectivity. Furthermore, the groups with the highest connectivity are found to have more likely encountered a major merger recently. These measurements are consistent with a scenario in which mergers might be responsible for populating the high connectivity bin. As mergers favour black hole growth (Hopkins et al. 2008; Schawinski et al. 2010; Dubois et al. 2016) and AGN activity, AGN feedback might be stronger in high connectivity groups and more efficient in quenching the BGG. Further measurements, including the black hole growth and AGN activity, gas inflows and outflows, BGG morphology, and redshift evolution of the signal, are still required to fully confirm this scenario. These measurements are beyond the scope of this paper and will be carried out in an upcoming work.

5 SUMMARY AND CONCLUSIONS

The number of filaments connected to a given group (within 1.5 times the virial radius) has been measured in COSMOS around X-ray-detected groups in the redshift range $0.5 < z < 1.2$.
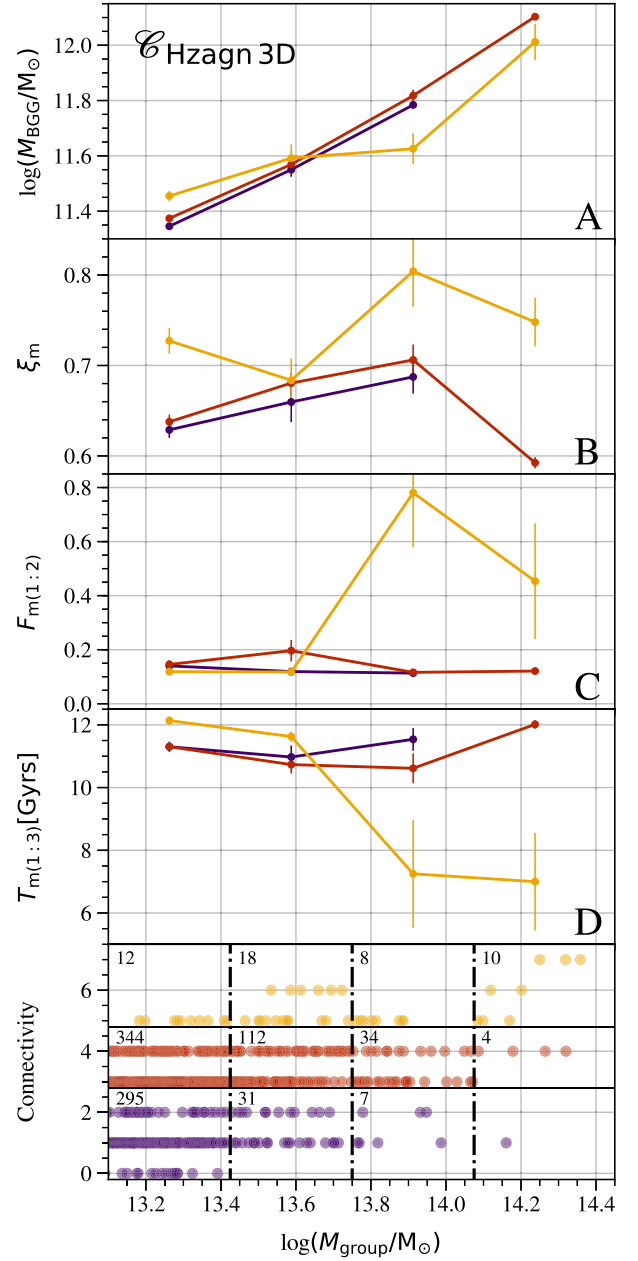

Figure 9. Group properties as a function of group mass in HORIZON-AGN, in three different connectivity bins. *Panel A*: mean BGG mass; *Panel B*: mean quenching efficiency due to AGN feedback; *Panel C*: fraction of groups with a major merger of ratio (1:2) during the last 6 Gyr; *Panel D*: mean time in Gyr since the last major merger of ratio (1:3). *Bottom panel*: the distribution of groups in bins of connectivity and group mass. The number of groups in each bin is indicated on the top left of the cell. The groups of a given colour set are used to build the curves of the same colour in the panels *A*, *B*, *C*, and *D*.

Its correlation with group mass, BGG mass and type has been investigated. The summary of our findings is as follows:

(1) In COSMOS, groups are found to be connected on average to two filaments, and up to four filaments. A small fraction of X-ray-detected groups do not lie at a peak of the galaxy distribution as extracted by DISPERSE;

(2) A mock photometric catalogue extracted from the HORIZON-AGN light-cone has been used to test the impact of photo-*z*

errors on connectivity. We found that connectivity is systematically underestimated when using photo-*z* with respect to exact redshifts. Conversely, the distribution of the connectivity in COSMOS and in the virtual mock photometric HORIZON-AGN catalogue agree well;

(3) Group mass and BGG mass increase with increasing group connectivity. This result is measured both in COSMOS and in HORIZON-AGN, and is in agreement with our current model of structure formation;

(4) At fixed group mass, the mass assembly of the BGG also depends on connectivity. Star-forming BGG are only found in groups of low and medium connectivity. At high group mass, groups with higher connectivity have a lower mass BGG than their counterpart with lower connectivity. A consistent result is found in HORIZON-AGN. In the simulation, AGN feedback quenching efficiency is higher at higher connectivity. Groups in the highest connectivity bin had on average a major merger more recently than at lower connectivity. Altogether, these findings suggest that different connectivity values trace different histories of group assembly;

(5) Given the correlation between group centre and projected skeleton nodes, our finding suggests that nodes of the 3D skeleton can also be used to predict the loci of X-ray groups, as originally suggested by Sousbie et al. (2011) for clusters.

These findings are qualitatively consistent both in simulations and observational data (see also Sarron et al. 2019, for consistent measurements in the CFHTLS). They underline the role played by the large-scale environment (as quantified by connectivity) in shaping a diversity of BGG properties. In particular they allow to shed light on some of the many questions still unanswered raised in the introduction, regarding to the location of the groups in the cosmic web, the scaling of connectivity with group mass and merger history, and the correlation between connectivity and AGN feedback. More observations will be needed to make these statements more statistically significant.

In closing, this study is a first step towards understanding the impact of the large-scale environment on group mass assembly. In order to know precisely what is the physical process beyond the measured correlation between connectivity and BGG mass and type, more detailed measurements from hydrodynamical simulations are essential. Upcoming 3D spectroscopic redshift surveys, including 4MOST (De Jong et al. 2012), DESI (DESI Collaboration 2016), PFS (Takada et al. 2014), MSE (McConnachie et al. 2016), provided they allow to extract reliable group catalogues, and photometric redshifts surveys including DES (Rykoff et al. 2016), *Euclid* (Laureijs et al. 2011), WFIRST (Spergel et al. 2013), LSST (LSST Dark Energy Science Collaboration 2012), KiDs (De Jong et al. 2013) will also prove crucial in extending this pilot study on larger sample and confirming the impact of large-scale environment on group mass assembly.

Beyond the implication for galaxy formation, cosmology would also benefit from group connectivity measurement as demonstrated by Codis et al. (2018). Although it is not possible to make a strong statement on the Dark Energy equation of state from the COSMOS data, the large-scale coverage of *Euclid* and LSST should allow such statistics.

REFERENCES

Alpaslan M. et al., 2016, MNRAS, 457, 2287
Arnouts S. et al., 2002, MNRAS, 329, 355
Aubert D., Pichon C., Colombi S., 2004, MNRAS, 352, 376
Beckmann R. S. et al., 2017, MNRAS, 472, 949
Behroozi P. S., Conroy C., Wechsler R. H., 2010, ApJ, 717, 379
Berlind A. A., Weinberg D. H., 2002, ApJ, 575, 587
Bertin E., Arnouts S., 1996, A&AS, 117, 393
Birnboim Y., Dekel A., 2003, MNRAS, 345, 349
Bonjean V., Aghanim N., Salomé P., Douspis M., Beelen A., 2018, A&A, 609, A49
Bruzual G., Charlot S., 2003, MNRAS, 344, 1000
Bullock J. S., Wechsler R. H., Somerville R. S., 2002, MNRAS, 329, 246
Byrd G., Valtonen M., 1990, ApJ, 350, 89
Capak P. et al., 2007, ApJS, 172, 99
Chabrier G., 2003, PASP, 115, 763
Chen Y.-C. et al., 2017, MNRAS, 466, 1880
Codis S., Pogosyan D., Pichon C., 2018, MNRAS, 479, 973
Comparat J. et al., 2015, A&A, 575, A40
Cooray A., Sheth R., 2002, Phys. Rep., 372, 1
Crone Odekon M., Hallenbeck G., Haynes M. P., Koopmann R. A., Phi A., Wolfe P.-F., 2018, ApJ, 852, 142
Danovich M., Dekel A., Hahn O., Teyssier R., 2012, MNRAS, 422, 1732
Danovich M., Dekel A., Hahn O., Ceverino D., Primack J., 2015, MNRAS, 449, 2087
Darvish B., Mobasher B., Sobral D., Hemmati S., Nayyeri H., Shivaei I., 2015, ApJ, 814, 84
de Jong J. T. A. et al., 2013, The Messenger, 154, 44
De Jong R. S. et al., 2012, in McLean I. S., Ramsay S. K., Takami H., eds, Proc. SPIE Conf. Ser.Vol. 8446, Ground-based and Airborne Instrumentation for Astronomy IV. SPIE, Bellingham, p. 84460T
DESI Collaboration, 2016, preprint (arXiv:1611.00036)
Di Matteo T., Springel V., Hernquist L., 2005, Nature, 433, 604
Di Matteo P., Combes F., Melchior A.-L., Semelin B., 2007, A&A, 468, 61
Dietrich J. P., Schneider P., Clowe D., Romano-Díaz E., Kerp J., 2005, A&A, 440, 453
Dietrich J. P., Werner N., Clowe D., Finoguenov A., Kitching T., Miller L., Simionescu A., 2012, Nature, 487, 202
Dubois Y., Devriendt J., Slyz A., Teyssier R., 2012, MNRAS, 420, 2662
Dubois Y., Pichon C., Devriendt J., Silk J., Haehnelt M., Kimm T., Slyz A., 2013, MNRAS, 428, 2885
Dubois Y. et al., 2014, MNRAS, 444, 1453

Dubois Y., Peirani S., Pichon C., Devriendt J., Gavazzi R., Welker C., Volonteri M., 2016, MNRAS, 463, 3948

Durret F. et al., 2016, A&A, 588, A69

Eckmiller H. J., Hudson D. S., Reiprich T. H., 2011, A&A, 535, A105

Finoguenov A. et al., 2007, ApJS, 172, 182

George M. R. et al., 2011, ApJ, 742, 125

Gobat R. et al., 2015, A&A, 581, A56

Gouin C., Gavazzi R., Codis S., Pichon C., Peirani S., Dubois Y., 2017, A&A, 605, A27

Gozaliasl G. et al., 2019, MNRAS, 483, 3545

Gunn J. E., Gott J. R., III, 1972, ApJ, 176, 1

Haardt F., Madau P., 1996, ApJ, 461, 20

Hahn O., Porciani C., Dekel A., Carollo C. M., 2009, MNRAS, 398, 1742

Hartley W. G., Conselice C. J., Mortlock A., Foucaud S., Simpson C., 2015, MNRAS, 451, 1613

Hearin A. P., Behroozi P. S., van den Bosch F. C., 2016, MNRAS, 461, 2135

Hopkins P. F., Cox T. J., Kereš D., Hernquist L., 2008, ApJS, 175, 390

Ilbert O. et al., 2006, A&A, 457, 841

Ilbert O. et al., 2009, ApJ, 690, 1236

Ilbert O. et al., 2013, A&A, 556, A55

Jauzac M. et al., 2012, MNRAS, 426, 3369

Jung I., Lee J., Yi S. K., 2014, ApJ, 794, 74

Kartaltepe J. S. et al., 2010, ApJ, 709, 572

Kauffmann G., Li C., Heckman T. M., 2010, MNRAS, 409, 491

Kauffmann G., Li C., Zhang W., Weinmann S., 2013, MNRAS, 430, 1447

Kaviraj S. et al., 2017, MNRAS, 467, 4739

Kereš D., Katz N., Weinberg D. H., Davé R., 2005, MNRAS, 363, 2

Kleiner D., Pimbblet K. A., Jones D. H., Koribalski B. S., Serra P., 2017, MNRAS, 466, 4692

Kraljic K. et al., 2018, MNRAS, 474, 547

Laigle C. et al., 2016, ApJS, 224, 24

Laigle C. et al., 2018, MNRAS, 474, 5437

Laigle C. et al., 2019, MNRAS, 486, 5104

Laureijs R. et al., 2011, preprint (arXiv:1110.3193)

Le Fèvre O. et al., 2015, A&A, 576, A79

Leauthaud A. et al., 2010, ApJ, 709, 97

Legrand L. et al., 2019, MNRAS, 486, 5468

Lilly S. J. et al., 2007, ApJS, 172, 70

LSST Dark Energy Science Collaboration, 2012, preprint (arXiv:1211.0310)

Luber N., van Gorkom J. H., Hess K. M., Pisano D. J., Fernández X., Momjian E., 2019, AJ, 157, 254

Luparello H. E., Lares M., Paz D., Yaryura C. Y., Lambas D. G., Padilla N., 2015, MNRAS, 448, 1483

Martin G., Kaviraj S., Devriendt J. E. G., Dubois Y., Laigle C., Pichon C., 2017, MNRAS, 472, L50

McConnachie A., Babusiaux C., Balogh M., Driver S., Côté et al., 2016, preprint (arXiv:1606.00043)

McCracken H. J. et al., 2012, A&A, 544, A156

Miyazaki S. et al., 2012, in McLean I. S., Ramsay S. K., Takami H., eds, Proc. SPIE Conf. Ser.Vol. 8446, Ground-based and Airborne Instrumentation for Astronomy IV. SPIE, Bellingham, p. 84460Z

Moore B., Katz N., Lake G., Dressler A., Oemler A., 1996, Nature, 379, 613

Parekh V., Durret F., Padmanabh P., Pandge M. B., 2017, MNRAS, 470, 3742

Peirani S. et al., 2017, MNRAS, 472, 2153

Peng Y.-j. et al., 2010, ApJ, 721, 193

Peng Y.-j., Lilly S. J., Renzini A., Carollo M., 2012, ApJ, 757, 4

Pichon C., Thiébaut E., Prunet S., Benabed K., Colombi S., Sousbie T., Teyssier R., 2010, MNRAS, 401, 705

Pichon C., Pogosyan D., Kimm T., Slyz A., Devriendt J., Dubois Y., 2011, MNRAS, 418, 2493

Poudel A., Heinämäki P., Tempel E., Einasto M., Lietzen H., Nurmi P., 2017, A&A, 597, A86

Power C., Navarro J. F., Jenkins A., Frenk C. S., White S. D. M., Springel V., Stadel J., Quinn T., 2003, MNRAS, 338, 14

Pozzetti L. et al., 2010, A&A, 523, A13

Reddick R. M., Wechsler R. H., Tinker J. L., Behroozi P. S., 2013, ApJ, 771, 30

Rykoff E. S. et al., 2016, ApJS, 224, 1

Salerno J. M., Martínez H. J., Muriel H., 2019, MNRAS, 484, 2

Sarron F., Adami C., Durret F., Laigle C., 2019, preprint (arXiv:1903.02879)

Schaap W. E., van de Weygaert R., 2000, A&A, 363, L29

Schawinski K., Dowlin N., Thomas D., Urry C. M., Edmondson E., 2010, ApJ, 714, L108

Scoville N. et al., 2007, ApJS, 172, 1

Scudder J. M., Ellison S. L., Mendel J. T., 2012, MNRAS, 423, 2690

Simha V., Weinberg D. H., Davé R., Gnedin O. Y., Katz N., Kereš D., 2009, MNRAS, 399, 650

Sousbie T., 2011, MNRAS, 414, 350

Sousbie T., Pichon C., Kawahara H., 2011, MNRAS, 414, 384

Spergel D. et al., 2013, preprint (arXiv:1305.5422)

Springel V., Di Matteo T., Hernquist L., 2005, ApJ, 620, L79

Sutherland R. S., Dopita M. A., 1993, ApJS, 88, 253

Takada M. et al., 2014, PASJ, 66, R1

Taniguchi Y. et al., 2007, ApJS, 172, 9

Taniguchi Y. et al., 2015, PASJ, 67, 104

Teyssier R., 2002, A&A, 385, 337

Tillson H., Miller L., Devriendt J., 2011, MNRAS, 417, 666

Treyer M. et al., 2018, MNRAS, 477, 2684

Tweed D., Devriendt J., Blaizot J., Colombi S., Slyz A., 2009, A&A, 506, 647

Vale A., Ostriker J. P., 2004, MNRAS, 353, 189

van de Voort F., Bahé Y. M., Bower R. G., Correa C. A., Crain R. A., Schaye J., Theuns T., 2017, MNRAS, 466, 3460

Weinmann S. M., van den Bosch F. C., Yang X., Mo H. J., 2006, MNRAS, 366, 2

Williams R. J., Quadri R. F., Franx M., van Dokkum P., Labbé I., 2009, ApJ, 691, 1879

Zaritsky D., White S. D. M., 1994, ApJ, 435, 599

Zehavi I., Contreras S., Padilla N., Smith N. J., Baugh C. M., Norberg P., 2018, ApJ, 853, 84

Zhang Y., Dietrich J. P., McKay T. A., Sheldon E. S., Nguyen A. T. Q., 2013, ApJ, 773, 115

APPENDIX A: COUNTING FILAMENTS IN COSMOS

A1 Impact of radius choice to measure connectivity

We check that our results do not depend on the chosen radius to measure the connectivity. The left-hand panel of Fig. A1 presents the mean connectivity as a function of group mass when measuring the connectivity within 1, 1.5, or 2 times the virial radius of the group. The solid line corresponds to the measurement chosen in the main text. This figure illustrates that the measured trend of increasing connectivity with group mass does not strongly depend on the chosen radius.

A2 Connectivity 1 versus 2

As discussed in Section 2.4, groups embedded in a filament which do not sit at a peak of the density field (i.e. which are not sitting on a node of the cosmic web) can in principle be assigned a connectivity of either $\mathcal{C} = 1$ (1a$-\mathcal{C}$) or $\mathcal{C} = 2$. However we also found that photo-z uncertainties tend to decrease connectivity. In other words, the fact that the group does not sit at a peak of the density field might just be due to shot noise driven by photo-z uncertainties. This
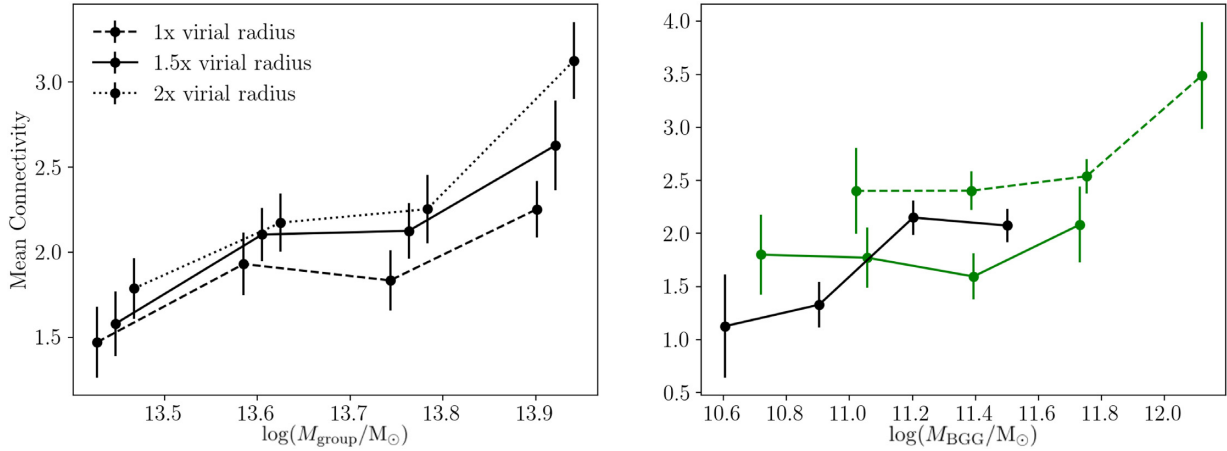
Figure A1. *Left:* Mean connectivity as a function of group mass, for different radii to measure connectivity in $\mathscr{C}_{cosmos}$. *Right:* Mean connectivity as a function of BGG mass when counting type-1b connectivity as connectivity 1 (instead of connectivity 2 as done in the main text) for $\mathscr{C}_{cosmos}$ (*black* line), $\mathscr{C}^{phot}_{Hzagn\,2D}$ (solid green line), and $\mathscr{C}^{phot}_{Hzagn\,2D}$ (dashed green line).

is confirmed by the fact that $1a-\mathcal{C}$ is not found when measuring the connectivity from the galaxy distribution with exact redshift. This fact has driven our choice to consider $1a-\mathcal{C}$ as $2-\mathcal{C}$ in the subsequent measurements.

The right-hand panel of Fig. A1 presents the measurement of mean connectivity versus BGG mass when considering $1a-\mathcal{C}$ as $1-\mathcal{C}$ (instead of $2-\mathcal{C}$, as was done in the right-hand panel of Fig. 5).

In this case, the strength of the signal (increase of connectivity for higher BGG masses) decreases when using photo-z (*solid* line) while it is unchanged when using the intrinsic redshift (*dashed* line).

This paper has been typeset from a TEX/LATEX file prepared by the author.